Direct Numerical Simulation on Mach Number and Wall Temperature Effects in the Turbulent Flows of Flat-Plate Boundary Layer

Xian Liang[1] and Xinliang Li[2,*]

[1] *School of Mathematics and Information Science, Beifang University for Nationalities, Yinchuan 750021, China.*
[2] *LHD, Institute of Mechanics, Chinese Academy of Sciences, No. 15 Beisihuanxi Road, Beijing 100190, China.*

Abstract. In this paper, direct numerical simulation (DNS) is presented for spatially evolving turbulent boundary layer over an isothermal flat-plate at $Ma_\infty = 2.25, 5, 6, 8$. When $Ma_\infty = 8$, two cases with the ratio of wall-to-reference temperature $T_w/T_\infty = 1.9$ and 10.03 are considered respectively. The wall temperature approaches recovery temperatures for other cases. The characteristics of compressible turbulent boundary layer (CTBL) affected by freestream Mach number and wall temperature are investigated. It focuses on assessing compressibility effects and the validity of Morkovin's hypothesis through computing and analyzing the mean velocity profile, turbulent intensity, the strong Reynolds analogy (SRA) and possibility density function of dilatation term. The results show that, when the wall temperature approaches recovery temperature, the effects of Mach number on compressibility is insignificant. As a result, the compressibility effect is very weak and the Morkovin's hypothesis is still valid for Mach number even up to 8. However, when Mach number equal to 8, the wall temperature effect on the compressibility is sensitive. In this case, when $T_w/T_\infty = 1.9$, the Morkovin's hypothesis is not fully valid. The validity of classical SRA depends on wall temperature directly. A new modified SRA is proposed to eliminate such negative factor in near wall region. Finally the effects of Mach number and wall temperature on streaks are also studied.

PACS: 47.27.E-, 47.27.nb, 47.40.Ki

Key words: Hypersonic, directly numerical simulation, compressibility effects, turbulent boundary layer, strong Reynolds analogy.

1 Introduction

Generally speaking, friction resistance and heat flux along the out-side metallic layer (skin) of high-speed aircraft increase sharply when the boundary layer changes from

---

Corresponding author. Email addresses: `liangxian@imech.ac.cn` (X. Liang), `lixl@imech.ac.cn` (X. L. Li)

laminar to turbulence. But there are two difficulties for drag reducing and heat degrading. One is how to predict transition region accurately, while another is to fully understand the inertial mechanism of compressible turbulent boundary layer (CTBL). The vortex structure and the inertial dynamics mechanism, which are closely related to CTBL, play a key role in the aero-industry [1]. The transition prediction is a popular subject of studying of boundary layer stability. The mechanism of CTBL which is another active studying area, will also be discussed in the present paper.

Direct numerical simulation (DNS) that involves the rapid development of computing technology is currently an important method in the study of turbulent mechanisms. In comparison with the results of experiment and theory, as what has been assessed by Schlatter et al. [2], DNS has the distinct advantage that all of the case-specific parameters (the inflow fields, boundary conditions and disturbances) can be set accurately, and no random measurement error corrupts the data that are obtained. High-order scheme always plays an important role in DNS of compressible boundary layer turbulence, especially at high Reynolds or with high Mach number. In order to numerically simulate such complex flow, various high-order and high resolutive schemes [3–7] have been developed in past decades. No doubt, WENO [8–10] and it's derived schemes are of the most successful ones. Especially, some low dissipative WENO type schemes have been proposed, such as compact-WENO [11, 12], WENO-Z [13], WENO-SYMBO [14], TWENO [15], which have been successfully used for multi-scales capture. As Pirozzoli [16] reviewed and suggested that the hybridization of a high-order compact scheme with the WENO scheme is good choice for the DNS and larger eddy simulation (LES) of turbulent compressible flows. Moreover, it is still an arduous work to enhance the robust or stability of such low dissipative and high resolutive methods, especially for the case of flow with high Mach number or high Reynolds number.

Recently, most of studies on the DNS for compressible turbulence focus on compressibility effects, especially on checking the validity of Morkovin's hypothesis [17]. This hypothesis indicates that, at a moderate free-stream Mach number (about $Ma_\infty \leq 5$), the dilatation is small, and any differences from incompressible turbulence can be considered by the mean variations in the fluid properties. Hitherto, this hypothesis is the basis for the analysis of compressible turbulence.

The DNS results of the spatial simulations for the CTBL with $Ma_\infty \leq 2.25$ over the flat-plate are proposed by Rai et al. [18], Pirozzili [19], Gatski [20], and Li [21], respectively. The results show that the essential dynamics of the CTBL greatly resemble the incompressible case. Pirozzli et al. [22] further to proposed the meticulous structure of a spatially evolving supersonic boundary layer by DNS with $Ma_\infty = 2$ up to $Re_\tau \approx 1120$. Such a result provides possibilities to start probing the effects of high Reynolds numbers.

Maeder et al. [23] investigated the effects of the Mach number and the wall temperature by using temporal simulations for the CTBL with $Ma_\infty = 3, 4.5, 6$, corresponding to a isothermal wall with $T_w/T_\infty = 2.5, 4.4, 7$, respectively, over a flat-plate boundary layer. In his computations, the wall temperature approximates recovery temperature. The results demonstrate that Morkovin's hypothesis and the strong Reynolds analogy (SRA)

are still valid when Ma_∞ up to 7 for different wall temperatures. Martin [24] and Duan et al. [25–27] proposed a series of investigations on CTBL over a flat-plate by using the temporally evolving DNS to assess the effects of wall temperature, the Mach number and high enthalpy on the Morkovin's hypothesis. In general, when $Ma_\infty = 5$, Morkovin's hypothesis is still valid for different wall temperatures, and with the wall temperature decreasing compressibility effects can be enhanced, but remain insignificant. Moreover, when the wall temperature approximates the recovery temperature, a similar conclusion can be drawn for free-stream Mach number changing from 0.3 to 12. Lagha et al. [28, 29] went further into this kind of research with wall temperature approaching recovery temperature by temporal evolution DNS. Liang [30, 31] proposed the DNS results of the spatially evolving boundary layer at Mach 8 over the flat-plate boundary layer.

In this article, a series of DNS of spatially evolving supersonic and hypersonic CTBL is presented. The purpose of the present study is to investigate the Mach number effects and the wall temperature effects and to assess the validity of the Morkovin's hypothesis.

2   Numerical methods and simulation parameters

2.1   Governing equations and numerical methods

In this paper, the Cartesian coordinate system is employed, with the x axis being the streamwise direction, the y axis being the normal-to-wall direction and the z axis being the spanwise direction. In order to capture the rapid change in the boundary layer, the finest mesh is employed in the fully developed turbulent region in streamwise. Meanwhile an exponential grid distribution is adopted along the wall-normal direction. The distribution function is defined as,

$$y(\eta) = \frac{e^{\eta b} - 1}{e^b - 1},\tag{2.1}$$

where $\eta \in [0,1]$ is computational region, b is stretch coefficient computed by

$$\frac{e^{\frac{b}{N-1}} - 1}{e^b - 1} = \frac{h_w}{L_y},\tag{2.2}$$

h_w is distance of the first grid point to the wall, N is total number of points, $y \in [0, L_y]$ is physical region in wall-normal region. In present paper, Eq. (2.2) is solved by using Newton iteration for unknown, b firstly. Then the distribution of grid is decided by Eq. (2.1) in wall-normal direction. It is considered at least three key factors that impact the distribution of grid in wall-normal direction. The first one is size of physical region. The second one is the distance of the first grid point to the wall. This value must be estimated beforehand and generally is set as one wall viscous lengthscale. The third one is the total nodes number. In present computation, there are at least 70 nodes are distributed in

Table 1: Basic grid mesh parameters for the DNS.

case	$L_x \times L_y \times L_z$	$N_x \times N_y \times N_z$	$\Delta x^+ \times \Delta y^+ \times \Delta z^+$
M2	$10 \times 0.68 \times 0.18$	$3195 \times 90 \times 256$	$10.1 \times 1.01 \times 7.2$
M5	$10 \times 0.68 \times 0.20$	$3980 \times 90 \times 256$	$10.4 \times 1.07 \times 4.9$
M6	$10 \times 0.68 \times 0.20$	$4450 \times 90 \times 256$	$6.82 \times 0.90 \times 3.9$
M8TH	$31 \times 0.70 \times 0.30$	$12460 \times 100 \times 320$	$12.2 \times 0.96 \times 4.6$
M8TL	$11 \times 0.70 \times 0.18$	$8950 \times 90 \times 640$	$11.2 \times 1.0 \times 4.5$

boundary layer. The first point near by the wall locates at about one viscous lengthscale. The details of mesh parameters can be found in Table 1.

Although low dissipative 7th-order hybrid WGVC-M7 [32] and 6th-order monotonicity-preserving optimized scheme (OMP6) [33] have been developed by our group at present, numerical computation becomes unstable when Mach number or Reynolds number increases rapidly. So the traditional 7th-order WENO [9] scheme is employed to approximate the convection terms in compressible NS equations in high Mach number case. Moreover, an enough fine grid distribution is considered to overcome the dissipation of present WENO. The viscous terms are approximated by using the 8th-order central difference scheme [34], and the third-TVD type Runge-Kutta method is used for advancing time. A two-dimensional laminar flat-plate boundary including the leading edge is simulated, and the computed two-dimensional results at $x = 4.0$ are used as the inflow conditions for a downstream three-dimensional computation. Non-reflect boundary conditions are used at the upper boundary and outflow boundary. Blow and suction disturbance are imposed at the wall in the interval $4.5 \leq x \leq 5.0$ for arousing the boundary layer transition early [19, 21].

2.2   Flow conditions and simulation parameters

To study the heat-transfer and Mach number effects on compressibility, the DNS of a spatially evolving CBLT is performed with a nominal freestream Mach number $Ma_\infty = 2.25, 5, 6, 8$ and a freestream temperature $T_\infty = 169.44 K$. An isothermal wall that is near to recovery temperature is set for $Ma_\infty = 2.25, 5, 6$ respectively. When $Ma_\infty = 8$, two kinds of wall temperature with $T_w / T_\infty = 1.9$ and 10.03 are further considered for investigating wall temperature effects. The other specific flow parameters are listed in Table 2, where δ is the thickness of the boundary layer (defined as the location at which the flow velocity is 99% of the free stream velocity); θ is the momentum thickness; $\delta_\nu = \nu \sqrt{\rho / \tau_w} = \nu / u_\tau$ is the viscous length scale; and u_τ is wall friction velocity. Table 2 also provides the different definitions of Reynolds numbers, where $Re_\infty \equiv \rho_\infty u_\infty l_\infty / \mu_\infty$ is based on the free stream; $Re_\theta \equiv \rho_\delta u_\delta \theta / \mu_\delta$ is based on the momentum thickness θ, the velocity, density and viscosity at the wedge of the boundary layer; $Re_\tau \equiv \rho_w u_\tau \delta / \mu_w$ is based on the boundary layer thickness, the friction velocity (u_τ) and the density and viscosity on the wall.

Table 2: Free steam, boundary-layer edge and wall parameters for the DNS. All of the statistical average values are obtained at fully developed turbulent region where $x=9.8,12.5,12.5,20.0$ and 14.5 for the case M2, M5, M6, M8TH and M8TL, respectively.

case	Ma_∞	Ma_δ	T_w/T_∞	T_w/T_r	Re_∞	Re_θ	Re_τ	δ	θ
M2	2.25	2.21	1.78	0.936	635000	6736	948	0.093	0.011
M5	5	4.73	5.0	0.917	2×10^6	19154	717	0.114	0.0109
M6	6	5.50	6.98	0.942	2×10^6	13146	413	0.092	0.0082
M8TH	8	7.08	10.03	0.809	5×10^6	46726	763	0.145	0.0128
M8TL	8	7.29	1.9	0.153	2×10^6	78000	2360	0.132	0.0135

In hypersonic flat-plate boundary layer flow, the recovery temperature is computed as

$$T_r = T_\infty \Big(1+\frac{\gamma-1}{2}Ma_\infty^2 r\Big), \tag{2.3}$$

where $r=Pr^\alpha$ is recovery factor with $\alpha=1/2$ for laminar case and $1/3$ for turbulence case. According to this equation, the wall conditions are close to adiabatic temperature for the cases M2, M5, and M6 in this paper. For the case M8TH, the wall temperature equals to $0.809T_r$, which is also very high. However, for the case M8TL, the wall temperature nears $0.153T_r$, which indicates very cold wall condition.

To assess the adequacy of the domain size, spanwise two-point correlations for the flow fields physics variables, such as density (ρ), velocity, (u,v,w), temperature (T), are computed. Fig. 1 shows the auto-correlations for streamwise velocity component at $y/\delta = 0.05,0.3$ and 0.75 for different cases. The results approach to zero in the middle part of the spanwise, which indicates that the spanwise domain size is large enough for computation.

Fig. 2 further to compare the skin friction of numerical results and theoretical ones. The later one is computed by [35]

$$C_f = \frac{0.455}{S^2}\left[\ln\Big(\frac{0.06}{S}Re_x\frac{1}{\overline{\mu}_w}\sqrt{\frac{1}{\overline{T}_w}}\Big)\right]^{-2}, \tag{2.4}$$

where $S=\frac{1}{\sin^{-1}A}\sqrt{\overline{T}_w-1}$ and $A=\big(r\frac{\gamma-1}{2}Ma_\infty^2\frac{1}{\overline{T}_w}\big)^{1/2}$. $\overline{\mu}_w$ and $\overline{T}_w$ are the average viscosity coefficient and the temperature on the wall, respectively, r is the correction coefficient, and x is the distance from the edge of the flat-plate boundary. The simulation shows good agreement with the results predicted by Eq. (2.4) in the fully turbulent region. Thus, the present simulation is reliable and valid.
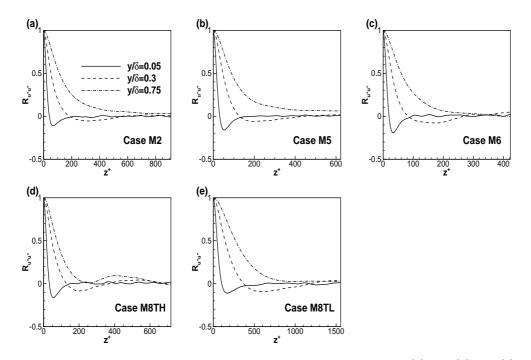
Figure 1: Spanwise two-point correlation for streamwise velocity component for (a) M2, (b) M5, (c) M6, (d) M8TH and (e) M8TL.
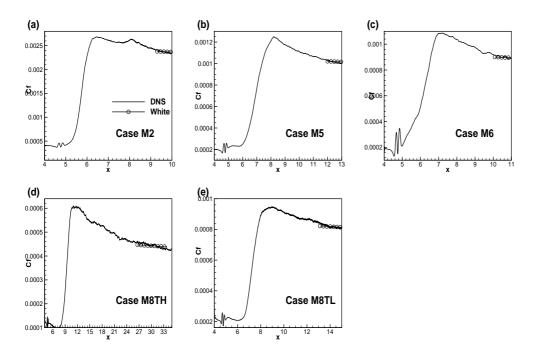

Figure 2: Skin friction distribution as function of x for (a) M2, (b) M5, (c) M6, (d) M8TH and (e) M8TL.

3 Turbulence statistics

3.1 Characteristics of mean flow

Generally, when the Mach number smaller than mediate value (generally ≤ 5), a van Direst transformed mean velocity profile is similar to incompressible case. The Van Direst transformation is defined as

$$\overline{u}_{vd}^{+} = \int_{0}^{\overline{u}^{+}} \left(\frac{\overline{\rho}}{\rho_w}\right)^{1/2} d\overline{u}^{+}, \tag{3.1}$$

where $\overline{u}^{+} = f(y^{+})$ is the mean velocity profile. The Fig. 3 shows that the Van Driest transformation collapses the profiles for different cases to the incompressible log law,

$$\overline{u}_{vd}^{+} = \frac{1}{\kappa}\ln y^{+} + C \tag{3.2}$$

with the Von Karman constant $\kappa = 0.41$ and different integral constant. Fig. 3 shows the mean velocity profiles. Table 3 gives the concrete parameter of mean velocity profiles. $Q1$, $Q2$ and $Q3$ denote intervals of the viscous sub-layer, buffer layer and log-law region, respectively. It indicates that when the wall temperature is near to the recovery temperature, the distribution of multilevel structure of CTBL is similar to the incompressible case for different Mach number. But when the wall temperature is very low for high Mach number case, such as M8TL, the region of viscous sub-layer shrinks, while the buffer layer enlargers and the log-law region moves far away from the wall. Such changes lead that the mean velocity profile is different from the incompressible case.
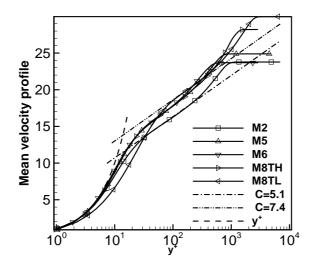

Figure 3: The Van Driest transformed velocity for different cases.

Table 3: Multilevel structure for mean velocity profile after Van Direst transformation.

case	κ	C	$Q1$	$Q2$	$Q3$
M2	0.41	5.1	[0,5]	[5,30]	[30,220]
M5	0.41	6.5	[0,5]	[5,35]	[35,120]
M6	0.41	6.5	[0,5]	[5,30]	[30,110]
M8TH	0.41	6.5	[0,5]	[5,40]	[40,115]
M8TL	0.41	7.4	[0,2]	[2,90]	[90,350]

3.2 Turbulent intensity

RMS (root-mean-square) of the velocity fluctuation, which is defined as $u'_{rms} = (\overline{u'u'})^{1/2}$ (similar to v'_{rms} and w'_{rms}) and is used to measure the intensity of the turbulence is showed versus y^+ in Fig. 4. In this figure the values of RMS are normalized by the local stream-wise mean velocity component $\overline{u}$ (or denoted as $\langle u \rangle$). The experimental results for the corresponding incompressible flat-plate boundary layer are denoted by symbols. It can be found that the compressible and incompressible data are in agreement with those in the near wall region (about for $y^+ < 30$) for the case M2, M5, M6 and M8TH. But there exists a large degree of dispersion for different cases when about $y^+ > 30$. Furthermore, there are distinct differences between the results for M8TL and the experiments, especially for the RMS of the streamwise velocity fluctuations which are shown in Fig. 4(a). Such differences are mainly caused by the limitation of wall coordinator y^+.
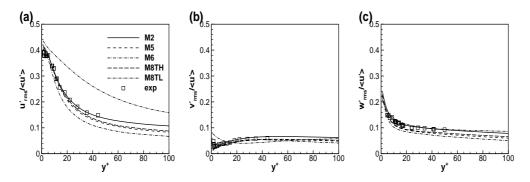

Figure 4: The RMS of the fluctuating velocity components *vs.* y^+ in (a) streamwise, (b) wall-normal and (c) spanwise.

So it is necessary to redraw the turbulent intensity versus a new wall coordinator. As being pointed in [30,41], the semi-local wall coordinate defined as $y^* = y[\tau_w \overline{\rho}(y)]^{1/2}/\overline{\mu}(y)$, which takes account of local flow fields information is adopted to redraw the turbulent intensity. Fig. 5 shows the turbulent intensity versus y^*, It is clearly shown that all the results for different cases collapsed and agree well with the experiments. Thus, the tur-bulent intensities are similar for different wall temperatures. Although the experiment
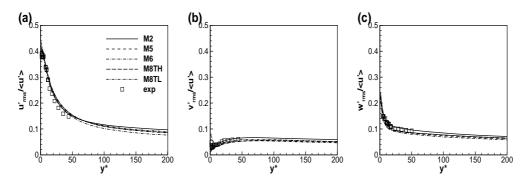
Figure 5: The RMS of the fluctuating velocity components *vs.* y^* in (a) streamwise, (b) wall-normal and (c) spanwise.

data are not enough, the tendencies of RMS of velocity perturbation conform with the results of the experiment.

3.3 Distribution of stress

The total shear stress (TSS) is defined as $\tau = -\overline{\rho u'v'} + \overline{\mu}(\partial\overline{u}/\partial y)$, where $-\overline{\rho u'v'}$ is the Reynolds stress (RS) and $\overline{\mu}(\partial\overline{u}/\partial y)$ is mean viscous shear stress (VSS). Fig. 6 compares the RS, VSS and TSS for different cases. It indicates that the VSS differs greatly for different cases, so does RS. Especially for M8TL, the buffer layer is enlarged obviously and moves away from the wall, which is consistent with the result of mean velocity profile. The tendencies of other curves for M2, M5, M6 and M8TH are almost the same generally. It can also be found that when about $y^+ > 50$, the VSS is nearer zero and the TSS that almost keeps constant when about $y^+ > 20$ mainly depends on the RS for M2, M5, M6 and M8TH.

Moreover, Fig. 7 demonstrates the RS, VSS and TSS *vs.* y^*. It is clearly shown that all curves collapse each other. The VSS is almost identical for the different cases. Thus, changing the wall temperature or the heat environment in the compressible boundary layer does not markedly impact the VSS. The difference in the TSS lies mainly in the RS. Fig. 7 shows that the RS increases more rapidly for the case of a strong cold wall (M8TL) than for other cases (M2, M5, M6 and M8TH), and its value is also bigger. Generally, the VSSs are almost independent of Mach number and wall temperature when about $y^* \lesssim 20$. The TSS almost keeps constant when about $y^* \gtrsim 30$, so does the RS. Such results are consistent with present conditions of zero-pressure-gradient through the boundary layer.

3.4 Heat flux and friction Mach number

In this paper, there are two inner layer parameters that are used to quantify changes of heat environment of isothermal simulations. The first one is the friction Mach number,
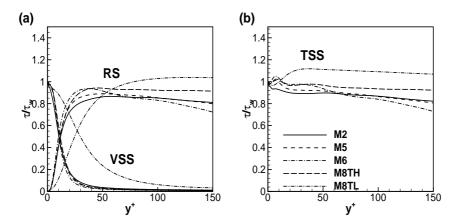
Figure 6: Comparison of the DNS results of (a) the Reynolds stress (RS), the mean viscous shear stress (VSS) and (b) the total shear stress (TSS) *vs.* y^+.
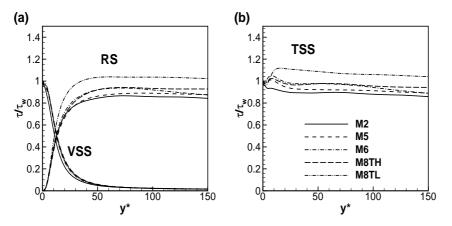

Figure 7: Comparison of the DNS results of (a) the Reynolds stress (RS), the mean viscous shear stress (VSS) and (b) the total shear stress (TSS) *vs.* y^*.

defined as $M_\tau = u_\tau/c_w$ where u_τ is the friction velocity and c_w is the speed of sound based on the wall temperature. After being further derived, $M_\tau = \sqrt{(\overline{\mu}\partial\overline{u}_w/\partial y)/(\overline{\rho}_w\overline{T}_w)}Ma_\delta$ (or $M_\tau^2 = C_f M_\delta^2/2$). Obviously, M_τ depends on Mach and Reynolds number and can be used to characterize compressibility. According to above stress analysis, the mean viscous stress seldom varies for different freestream Mach numbers. So M_τ increases with freestream Mach number increasing or with wall temperature decreasing. The second parameter is wall heat flux whose nondimensional form can be written as $Q_w = -(\partial\overline{T}/\partial y)_w/(\mathrm{Pr}R_{\delta_{99}}\rho_w u_\tau)$ [36,37]. When the heat transfers from the flow to the wall, the value of Q_w is negative, while it is positive when the wall is heating the flow.

In the case of compressible boundary layer flows over a zero-pressure-gradient flatplate, the mean pressure approximately keeps constant in the boundary layer. And then
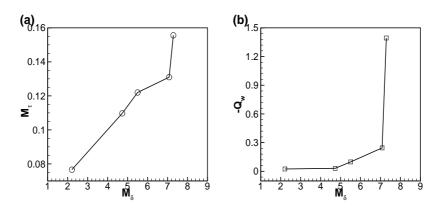
Figure 8: The changes of (a) friction Mach number, M_τ, and (b) negative non-dimensional heat flux, $-Q_w$, vs. M_δ.

the mean density is approximately in inverse ratio to the temperature. For the supersonic or hypersonic boundary-layer flows with the given free-stream Mach number, to lower the wall temperature will increase the wall heat flux as well as the near-wall temperature gradient, and increase the frication Mach number, and then enhance the compressibility effects of the near wall flow.

M_τ and Q_w are listed in Table 4 for different cases. Fig. 8 further shows the changes of M_τ and Q_w vs. the M_δ (a Mach number at the outer edge of boundary layer). When wall temperature approaches the recovery temperature (such as case of M2, M5, M6 and M8TH), the friction Mach number increases with Mach number increasing. Meanwhile, the absolute value of heat flux has the similar change law. As showed in Fig. 8, M_τ and $|Q_w|$ are more sensitive to the wall temperature than to the Mach number. It indicates that cooling the wall enhances the compressibility effect obviously when Mach number equals 8.

Table 4: The friction Mach number and nondimensional heat flux.

case	M2	M5	M6	M8TH	M8TL
M_τ	0.0766	0.1097	0.122	0.131	0.1556
Q_w	-0.0243	-0.0317	-0.0981	-0.245	-1.394

4   Reynolds analogies

Strong Reynolds analogy proposed by Morkovin [17] (called classical SRA) gives the relationship between velocity and temperature with premise that the total temperature keeps constant and its fluctuation nears zero. In this part, the classical SRA and some modified SRA are to be evaluated. Furthermore, a new improved SRA based on present DNS data is presented.

4.1 Validation of classical SRA

One of the classical SRA can be given as,

$$\frac{T''_{rms}/\widetilde{T}}{(\gamma-1)Ma^2(u''_{rms}/\widetilde{u})} \approx 1, \tag{4.1}$$

where $Ma^2 = \widetilde{u}^2/(\gamma R\widetilde{T})$ is a local Mach number. In further developments that are based on considering the influence of the heat flux on the wall or eliminating the influence of the wall temperature, modified SRA relations have been proposed over recent decades. For example, Cebeci and Smith [38] derived an extended SRA (ESRA) based on Eq. (4.1):

$$\frac{T''_{rms}/\widetilde{T}}{(\gamma-1)Ma^2(u''_{rms}/\widetilde{u})} \approx \left[1 + C_p \frac{\widetilde{T}_w - \widetilde{T}_{t\delta}}{\widetilde{u}\widetilde{u}_\delta}\right], \tag{4.2}$$

where T_t denotes the total temperature. SRA and ESRA agree well with experiments for boundary layers with adiabatic walls. However, Gaviglio [39] pointed out that SRA and ESRA are not adequate for isothermal wall flows. This point has been verified by the present study. Gaviglio [39], Rubesin [40] and Huang [41] also proposed modified SRA relations, denoted GSRA, RSRA and HSRA, which correspond to $c = 1.0$, $c = 1.34$ and $c = Pr_t$, respectively, in the following Eq. (4.3):

$$\frac{T''_{rms}/\widetilde{T}}{(\gamma-1)Ma^2(u''_{rms}/\widetilde{u})} \approx \frac{1}{c[1 - \partial\widetilde{T}_t/\partial\widetilde{T}]}. \tag{4.3}$$

The relations (4.1), (4.2) and (4.3) indicate ratios near 1 if Morkovin's hypothesis is valid. Fig. 9 shows the classical SRA and the modified SRA. The Fig. 9(a)-(c) indicate that all kinds of SRA are near 1, except that the RSRA has the largest deviation. Such results prove that the Morkovin hypothesis is still valid for case M2, M5, M6. This is mainly because the wall temperature is near recovery temperature so that there is not enough (or even zero) heat flux on the wall.

Furthermore, Fig. 10 shows that the total temperatures, defined as $\widetilde{T}_t = \widetilde{T} + \widetilde{u}_i\widetilde{u}_i/(2c_p)$, keep constant for the case M2, M5 and M6 through the boundary layer. Meanwhile, the amplitudes of their fluctuations almost decrease 2 orders, approximating to zero. As a result, in such case, the basic premise for validation of SRA and Modified SRA is true. Fig. 10 also shows that the total temperature has a certain extent of change for M8TH. As a result, the value of SRA is near 0.7, up to 30% deviation from unit. Moreover, as shown in Fig. 10(a), the total temperature for M8TL has distinctive changes and almost no longer keeps constant. Meanwhile, as shown in Fig. 10(b), total temperature fluctuation has at least 25% relative deviation comparing to itself. It is large enough to break the premise of the validation of SRA. Finally, as shown in Fig. 9(e), the value of classical SRA is near 0.2 which is far away from 1. Moreover, the GSRA, RSRA and HSRA fail to provide reasonable predicted results for about $y^+ < 90$. Thus, Mokovin's hypothesis is no longer totally valid for M8TL.
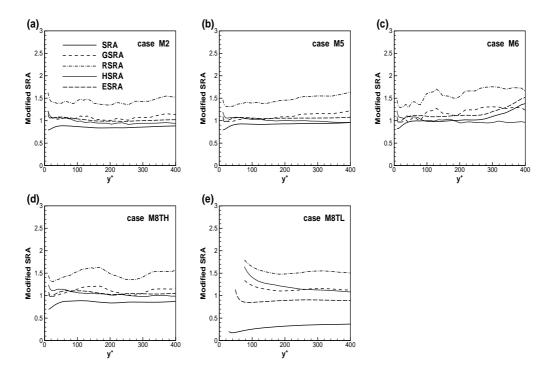
Figure 9: Distribution of SRA, ESRA, GSRA, RSRA, and HSRA *vs.* y^+ for (a) M2, (b) M5, (c) M6, (d) M8TH and (e) M8TL.
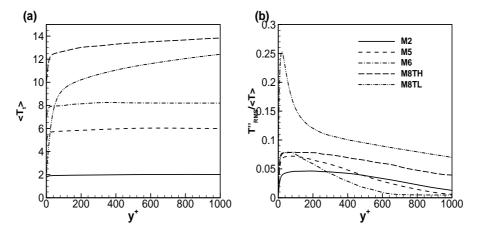

Figure 10: Total temperature and its fluctuation (normalized by local total temperature).

Generally, for different Mach number, even up to 8 (as case M8TH), if wall temperature is near recovery temperature, it does not lead to an enough strong compressibility effect in the near-wall region, and Morkovin's hypothesis is still valid to a great extent.

4.2 New modification of SRA

The overall appearance of classical SRA, as shown in Fig. 9, the predicted value is close to 1 when the wall temperature nears recovery temperature. It also decreases with the wall cooling. So a modified term which relates to the recovery temperature (or freestream Mach number) and wall temperature is necessary to be considered and added into classical SRA formula. A new modified form can be written as

$$\frac{T''_{rms}/\widetilde{T}}{(\gamma-1)Ma^2(u''_{rms}/\widetilde{u})} \approx \left(\frac{T_w}{T_r}\right)^{\omega} = \beta^{\omega}, \tag{4.4}$$

where T_w and T_r are wall temperature and recovery temperature, respectively. The definition of T_r, which relates to freestream Mach number, can be found in Eq. (2.3). ω, which is a function of total temperature or static temperature, changes from 0 to 1. The present analysis indicates that it can also be simply set as a constant. It equals to 0.7 and work well in present paper. This new modified form is called LSRA in this paper. When the wall is adiabatic, $\beta = 1$, and Eq. (4.4) degenerates to Eq. (4.1), denoting form of classical SRA; when the wall is cooled ($T_w < T_r$), $0 < \beta < 1$ and approaches 1 with wall temperature closing to adiabatic case, and approaches 0 with wall temperature decreasing towards 0. As a result, the curve of classical SRA is moved upwards to be close to 1. Contrarily, when the wall is heated and wall temperature is higher than recovery temperature, $\beta > 1$, the curve of classical SRA is moved downwards to 1.

Fig. 11 shows the results of HSRA, ESRA and LSRA. LSRA can provide more accurately predicted results with a comparatively simplified improvement. The results show that LSRA can eliminate the wall temperature influence and provide more precise results. Moreover, as shown in Fig. 11(a)-(d), the results of HSRA for case M2, M5 M6 and M8TH are more accurate than ESRA and LSRA. However, when the wall is very cold (case M8TL), as shown in Fig. 11(e), ESRA and LSRA give better predicted results than HSRA in near-wall region.

4.3 Validation of other forms of SRA

Besides the classical expression of SRA shown by Eq. (4.1), three other expressions are listed below:

$$R_{u''T''} \approx -1, \tag{4.5}$$

$$R_{u''v''} = -R_{v''T''}\left[1 - \frac{\overline{v''T''_t}}{\overline{v''T''}}\right], \tag{4.6}$$

$$Pr_t = \frac{\overline{\rho u''v''}(\partial\widetilde{T}/\partial y)}{\overline{\rho v''T''}(\partial\widetilde{u}/\partial y)} \approx 1. \tag{4.7}$$

Pr_t, the turbulent Prandtl number, is a measure of the ratio of the turbulent kinematic momentum transfer over the turbulent kinematic heat transfer.
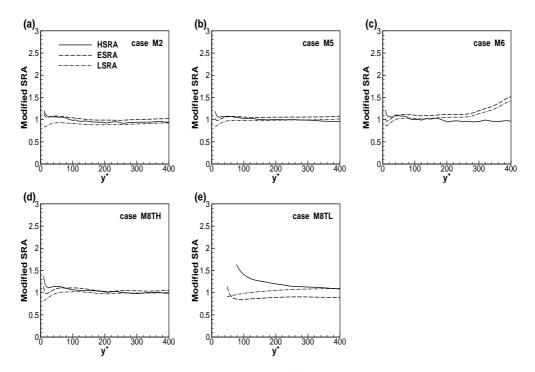
Figure 11: Distribution of HSRA, ESRA and LSRA *vs.* y^+ for (a) M2, (b) M5, (c) M6, (d) M8TH and (e) M8TL.

Eq. (4.5) indicates that $u^{''}$ and $T^{''}$ have a negative correlation. As shown in Fig. 12(a), when the wall temperature nears recovery temperature (case M2, M5, M6, M8TH), the distributions of $R_{u^{''}T^{''}}$ are almost irrelevant to the Mach number. However, the wall temperature impacts the distribution seriously for the case of high Mach number. Moreover, Fig. 12(a) indicates that there exist obvious differences when about $y^+ \lesssim 100$ in the distributions between M8TL and other cases. In the present investigation, it is shown that $u^{''}$ and $T^{''}$ are not completely anti-correlated. $R_{u^{''}T^{''}}$ equals approximately -0.6 through the most parts of boundary layer.

Additionally, according to the Morkovin's hypothesis, the total temperature fluctuation equals to zero through the boundary layer, so Eq. (4.6) implies that $R_{u^{''}v^{''}}$ and $R_{v^{''}T^{''}}$ are strongly contrary according to the classical SRA. As shown in Fig. 12(b), the curves not only test such contrary nature, but also indicate that the correlation of $v^{''}$ and $T^{''}$ is relatively weak ($R_{v^{''}T^{''}} \approx 0.4$), as well as the anti-correlation of $u^{''}$ and $v^{''}$ ($R_{u^{''}v^{''}} \approx -0.4$).

It is necessary to highlight that there are distinctive differences in the distribution of $R_{u^{''}T^{''}}$ (as well as $R_{v^{''}T^{''}}$ and $R_{u^{''}v^{''}}$) between the case M8TL and other cases in the near-wall region. This further indicates that very cold wall condition can cause large impacts on SRA.

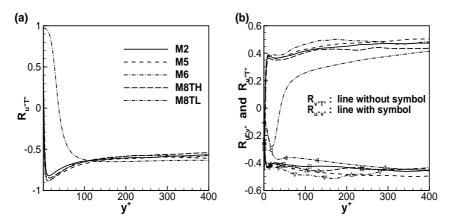Similar to the definition of Pr_t, the Prandtl number for turbulent mass diffusion, Pr_ρ,

Figure 12: Comparison of correlations of (a) $R_{u''T''}$, (b) $R_{u''v''}$ and $R_{v''T''}$.
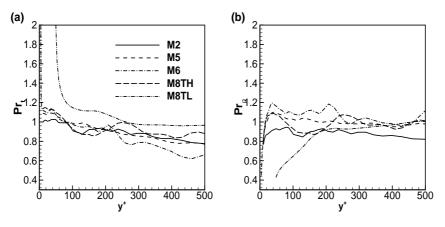

Figure 13: Comparison of (a) Pr_t and (b) Pr_ρ.

is defined as

$$Pr_\rho = \frac{-\overline{u''v''}(\partial\overline{\rho}/\partial y)}{-\overline{\rho'v''}(\partial\widetilde{u}/\partial y)}.\tag{4.8}$$

Pr_ρ is a measure of the ratio of the turbulent kinematic viscosity over the turbulent mass diffusivity. Morkovin's hypothesis also implies that Pr_t and Pr_ρ approximate 1 [6,8]. Fig. 13 depicts the distributions of the Pr_t and Pr_ρ. It shows that the very cold wall impacts Pr_t and Pr_ρ seriously for about $y^+ \lesssim 200$. The values of them are far away from 1. When about $y^+ \gtrsim 200$, $\text{Pr}_t \approx \text{Pr}_\rho$ and approximates to the order 1. Meanwhile, the figure also shows that the Mach number does not influence the distribution of Prandtl number when wall temperature nears to recovery temperature, as in case M2, M5, M6 and M8TH. At the same time, Pr_t and Pr_ρ vary from 0.8 to 1.1 in the most parts of the boundary layer.

5 Compressibility

Compressibility effect is an important area in studying the CTBL. It has been investigated from different angles [26, 31, 42]. It is closely related to noise, shocklet and heat flux in hypersonic shear turbulence. In this part, the compressibility effect is studied through investigating the turbulent Mach number, fluctuating Mach number, dilatation term. Some similar analysis can be found in Subsection 3.4.

5.1 Turbulent Mach number and perturbation Mach number

In turbulent fields, a sound time scale [43] is defined as $\tau_a = \Lambda/\overline{a}$, where Λ is a characteristic scale of average length of fluctuation moment, an integral scale for instance; and $\overline{a}$ is local average sound speed. τ_a denotes the characteristic time scale of sound wave propagation. Moreover, multi-scale turbulent fields consist of different scales vortexes, and their interactions. The turbulent characteristic time scale [44] (or called characteristic time scale of energy-containing moment) is defined as $\tau_t = k/\varepsilon$, where $k = \overline{u_i' u_i'} = q'^2$ is twice of turbulent kinetic energy, and $\varepsilon = q'^3/\Lambda$, is average dissipation rate. $q' = \sqrt{\overline{u_i' u_i'}}$ is the RMS (root mean square) of the fluctuating velocity. τ_t is a time scale of energy-containing turbulent vortex. It denotes that the energy-containing turbulent vortex transfers the most of energy to smaller scale turbulent vortex after τ_t. Furthermore, the turbulent Mach number can be defined as

$$M_t = q'/\overline{a} = \tau_a/\tau_t. \tag{5.1}$$

So M_t, which is based on the fluctuating velocity and local average sound speed, denotes the ratio of the characteristic time scale of sound wave propagation over the turbulent characteristic time scale. It characterizes the internal compressibility effects in compressible turbulent fields. Morkovin's hypothesis points out that when M_t is very small, the compressibility effects are mainly reflected by influencing mean flow. When M_t is near order 1 or $\tau_a \geq \tau_t$, it means that the amplitude of velocity fluctuation reaches or exceeds sound speed order, thus, unsteady shocklet and enough strong internal compressibility effects can be induced.

Moreover, in some special cases, such as aero-acoustic turbulence, fluctuation of $T'/\overline{T}$ is more important than M_t to dominate the compressibility. Based on such consideration, the RMS perturbation of the local Mach number is examined. It is called the fluctuating Mach number M' that characterizes local changes in compressible turbulent fields.

Fig. 14(a) and (b) show M_t and M'_{RMS} for different cases, respectively. Here the semi-local coordinator y^* is employed for collapsing the positions of peak values of different curves. Fig. 14(a) indicates that there is only one extreme point on each curve for M_t at about $y^* \approx 17$. When the wall is very cold (as case M8TL), the maximum of M_t approaches 0.6 at the near-wall region, which is big enough to produce strong compressibility effect. For M8TH, the maximum is about 0.4, which is even slightly less than 0.42 for M6. Such
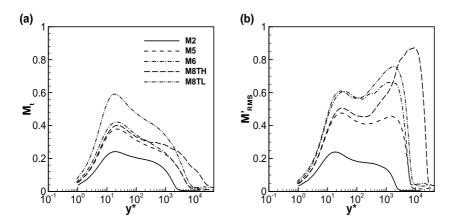
Figure 14: Distribution of (a) turbulent Mach number and (b) fluctuating Mach number *vs.* y^*.

results obviously indicate that Mach number is not the only factor to decide compressibility effect. The wall temperature, freestream Mach number and combined action should be counted as a whole in the investigation.

As shown in Fig. 14(b), there are two extreme points (except case M2, denotes low freestream Mach number case) on the curves of M'_{RMS}. One lies in about $y^* \approx 30$, (except $y^* \approx 17$ for M2) another lies near by the edge of boundary layer. So the strong temperature fluctuation as occurs at above two regions is different from the position of extreme point of M_t. The results show that $M'_{RMS} > 0.45$ for M5, M6, M8TL and M8TH in near-wall region. And it is bigger than 0.65 for M6, M8TH and M8TL at the edge of boundary layer, even up to 0.9 for M8TH.

Generally, M_t and M'_{RMS} increase with freestream Mach number increasing, or wall cooling, which further enhances the compressibility effect.

5.2 Dilatation term

The dilatation term $\vartheta = \nabla \cdot V'$ is another important characteristic variable that is associated with compressible effects. It is zero for an incompressible flow and very small for a low free-stream Mach number. As is well known, the dilatation procedure correlates with the change of the mean density, and therefore, the density increases when $\vartheta < 0$, which denotes a compression procedure, or it decreases with $\vartheta > 0$ which denotes a dilatation procedure. In other words, the density can also be used to normalize the dilatation term. Therefore, the probability density functions (PDF) of ϑ and $\langle \rho \rangle \vartheta$ are to be computed for assessing the compressibility. Figs. 15-17 indicate the PDF of ϑ and $\langle \rho \rangle \vartheta$ at $y = 0.1\delta$, 0.5δ and 0.9δ, respectively. The results show that, besides some slight deviation in near wall region, the compression and dilatation procedures are almost equal probability as a whole. The PDF of these two procedures follows the normal distribution. Moreover, they are more active in near wall region than in far away from wall region.
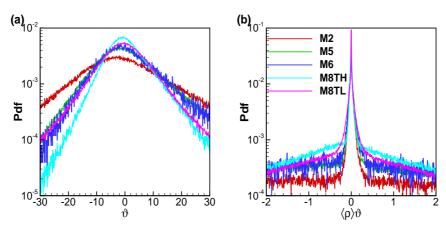
(a)

(b)

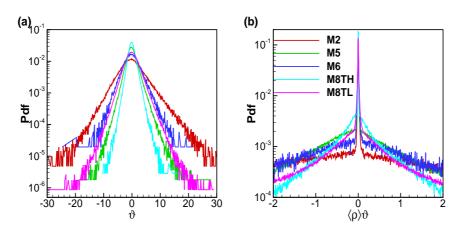Figure 15: The PDF of the dilatation term at $y = 0.1\delta$.

(a)

(b)

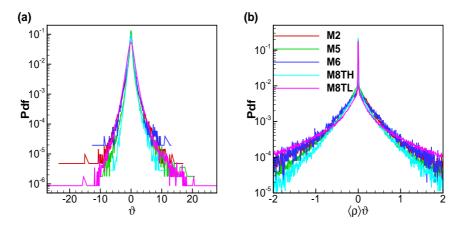Figure 16: The PDF of the dilatation term at $y = 0.5\delta$.

(a)

(b)

Figure 17: The PDF of the dilatation term at $y = 0.9\delta$.

6 Near-wall turbulent structure

The Mach number and the wall temperature effects on the near-wall streaks is further investigated. Fig. 18 shows the distributions of the instantaneous streamwise velocity component along the spanwise direction at about $y^+ \approx 15$. The present visual region covers 8δ long in the streamwise and one δ wide in the spanwise directions for each case. This region lies in the fully developed turbulent region.

There are some distinctive features in the present results, Firstly, the streaks (deep color structure) along the streamwise direction become flatter with the free-stream Mach number increasing for wall temperature near recovery temperature. Meanwhile, they have similar law, as well as reduction of wall temperature for the same free-stream Mach number. Fig. 18 indicates that the streaks for M6 are flatter than those for M2 (or M5). And also they are flatter for M8TL than for M8TH. According to previous analysis, this trend is the result of the enhancement of a compressibility effect. Secondly, the streaks are retained longer either for a higher Mach number case or for a colder wall case. The figure
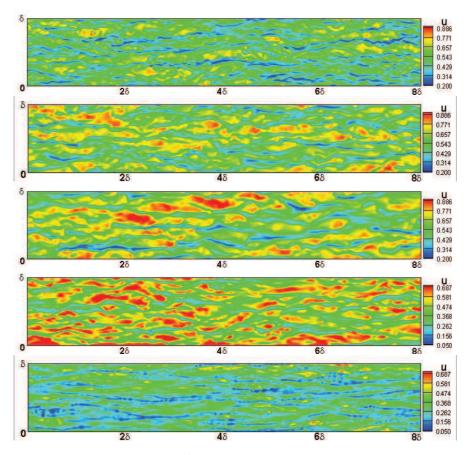

Figure 18: The near-wall streaks at about $y^+ \approx 15$ for M2, M5, M6, M8TH and M8TL (from up to down).
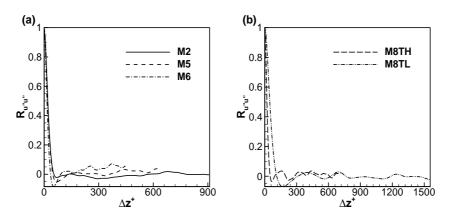
Figure 19: Two-point correlation *vs.* Δz^+ at $y^+ \approx 15$.

indicates that the steaks for M8TL are obviously longer than those for M2, M5 and M6 and M8TH. Thus, reducing the wall temperature increases the stream-wise coherency of near-wall streaks.

Thirdly, the average spanwise spacing (ASS) of streaks slightly increase with an increase in free-stream Mach number. This can be found in Fig. 19, where the auto-correlation coefficients of $u^{''}$ along spanwise at about $y^+ \approx 15$ is employed to check the ASS. Table 5 shows some approximate values of ASS. As shown in Fig. 19(a) and Table 5, the ASSs are equal to about 100 wall units for M2, M5, M6 and M8TH. Such results are similar to the traditional ones [45, 46] (approximately 100 wall units) for incompressible case. Fig. 19(b) shows that the ASS of near-wall streaks increase significantly with a decrease in wall temperature when Mach number equals 8. The present value of ASS for M8TL is much bigger than the traditional one. Table 5 also indicates that the ASS increases with growing distance from the wall.

Table 5: The average spanwise spacing of streaks.

case	$y^+ \approx 4$	$y^+ \approx 15$
M2	90.0	113.6
M5	103.7	124.5
M6	105.3	127.1
M8TH	119.7	130.6
M8TL	239.4	259.3

7 Conclusions

The investigation on the spatially evolving turbulent boundary layer over flat-plates with Mach 2.25, 5, 6 and 8 have been performed by DNS. The effects of Mach number and wall

temperature on the compressibility and the turbulent statistical characteristics have been analyzed. Some conclusions have been drawn as follows.

The compressibility effects are insignificant when the wall temperature nears the recovery temperature with Mach number up to 8, such as M2, M5, M6 and M8TH. In such cases, the compressibility effects are enhanced slightly with freestream Mach number increasing. As a result, the mean velocity profiles with Van Driest transformation are similar to incompressible case. The Mach number and the wall temperature impact on the mean viscosity shear stress (VSS) insignificantly, but on the Reynolds stress (RS) significantly. Furthermore, an increase in the total shear stress (TSS) is mainly caused by an increase in the Reynolds stress which increases with freestream Mach number increasing or wall cooling.

The strong Reynolds analogy (SRA) depends greatly on the wall temperature in high Mach number case. The validity of the SRA degrades with wall temperature decreasing. It is still valid for the case M2, M5, M6 and M8TH. In such cases, the total temperatures are almost invariant through the boundary layer and their fluctuations are relatively very small, at least less than 2 orders. However, the classical SRA and modified SRA are not totally valid for the case of M8TL, a very cold wall case, when about $y^+ < 100$ where the total temperature has dramatically change and amplitude of its fluctuation is as large as 25% relatively. Due to considering the effects of the wall temperature, free-stream Mach number and combined action, the present modified model (LSRA) improves the predicted accuracy, even for very cold wall case.

When the wall temperature is near to the recovery temperature, the average spanwise space (ASS) slightly increases with Mach number increasing, and the values mainly lie in interval $(90,120)$ for $y^+ \approx 4$ and $(110,130)$ for $y^+ \approx 15$. This is the similar to incompressible case. Moreover, the ASS increases with wall cooling, even up to 260 for the very cold wall case (case M8TL).

The results of turbulent Mach number, perturbation Mach number, friction Mach number, dilatation term and heat flux along the wall show that the compressibility effects increase slightly with Mach number increasing for case M2, M5, M6 and M8TH. And when Mach number is up to 8, the compressibility effects increase with decreasing wall temperature, which has been partly discussed in reference [31].

Further investigation on effects of Mach number, wall temperature and combined action on extended self-similarity (ESS), scale law, transition and spatial evolution of flow structure are in the process.

Acknowledgments

References

[1] E. F. Spina, The physics of supersonic turbulent boundary layers, Annu. Rev. Fluid Mech., 26(1994), 287-319.

[2] P. Schlatter and Örlü, Assessment of direct numerical simulation data of turbulent boundary layers, J. Fluid Mech., 659(2010), 116-126.

[3] S. K. Lele, Compact Finite Difference Schemes with Spectral-like Resoution, J. Comput. Phys., 103(1992), 16-42.

[4] D. X. Fu and Y. W. Ma, A high-order accurate difference scheme for complex flow fields, J. Comput. Phys., 134(1997), 1-15.

[5] Z. F. Tian and S. Q. Dai, High-order compact exponential finite difference methods for convection-diffusion type problems, J. Comput. Phys., 220(2007), 952-974.

[6] X. G. Deng, M. L. Mao, G. H. Tu, H. X. Zhang and Y. F. Zhang High-order and high accurate CFD methods and their applications for complex grid problems, Commun. Comput. Phys., 11(2012), 1081-1102.

[7] B. van Leer, Upwind and high-resolution methods for compressible flow: From donor cell to residual-distribution schemes, Commun. Comput. Phys., 1(2006), 192-206.

[8] C. W. Shu, Essentially non-oscillatory and weighted essentially non-oscillatory schemes for hyperbolic conservation laws, ICASE/NASA Tech. CR(1997), Technical Report 206253.

[9] G. S. Jiang and C. W. Shu, Efficient implementation of weighted ENO schemes. J. Comput. Phys., 126(1996), 202-228.

[10] D. Balsara and C. W. Shu, Monotonicity preserving weighted essentially non-oscillatory schemes with increasingly high order accuracy, J. Comput. Phys., 160(2000), 405-452.

[11] Y. X. Ren, M. Liu and H. Zhang, A characteristic-wise hybrid compact-WENO scheme for solving hyperbolic conservation laws, J. Comput. Phys., 192(2003), 365-386.

[12] S. Pirozzoli, Conservative hybrid compact-WENO schemes for shock-turbulence interaction, J. Comput. Phys., 178(2002), 81-117.

[13] C. Marcos, C. Bruno and S. D. Wai, High order weighted essentially non-oscillatory WENO-Z schemes for hyperbolic conservation laws, J. Comput. Phys., 230(2011), 1766-1792.

[14] M. P. Martin, E. M. Taylor, M. Wu and V. G. Weirs, A bandwidth-optimized WENO scheme for the effective direct numerical simulation of compressible turbulence, J. Comput. Phys., 220(2006), 270-289.

[15] J. Zhu and J. X. Qiu, Trigonometric WENO schemes for hyperbolic conservation laws and highly oscillatory Problems, Commun. Comput. Phys., 8(2010), 1242-1263.

[16] S. Pirozzoli, Numerical methods for high-speed flows, Annu. Rev. Fluid Mech., 43(2011), 163-194.

[17] M. V. Morkovin, Effects of compressibility on turbulent flows, In A. Favre, editor, Macutee canique de la Turbulence, CNRS(1962), 367-380.

[18] M. M. Rai, T. B. Gatski and G. Erlebacher, Direct simulation of spatially evolving compressible turbulent boundary layers, AIAA Paper, 1995-0583(1995).

[19] S. Pirozzoli and F. Grasso, Direct numerical simulation and analysis of a spatially evolving supersonic turbulent boundary layer at M=2.25, Phys. Fluids, 16(2004), 530-545.

[20] T. B. Gatski and G. Erlebacher, Numerical simulation of a spatially evolving supersonic turbulent boundary layer, NASA Tech. TM(2002), 211934.

[21] X. L. Li, D. X. Fu, Y. W. Ma, Direct numerical simulation of a spatially evolving supersonic turbulent boundary layer at Ma=6, Chin. Phys. Lett., 23(2006), 1519-1522.

[22] S. Pirozzoli and M. Bernardini, Turbulence in supersonic boundary layers at moderate

Reynolds number, J. Fluid Mech., 688(2011), 120-168.

[23] T. Maeder, N. A. Adams and L. Kleiser. Direct simulation of turbulent supersonic boundary layers by an extended temporal approach, J. Fluid Mech., 429(2001), 187-216.

[24] M. P. Martin, DNS of hypersonic turbulent boundary layers, AIAA Paper(2004), 2004-2337.

[25] L. Duan, I. Beekman and M. P. Martin, Direct numerical simulation of hypersonic turbulent boundary layers. part 2. effect of wall temperature, J. Fluid Mech., 655(2010), 419-445.

[26] L. Duan, I. Beekman and M. P. Martin, Direct numerical simulation of hypersonic turbulent boundary layers. part 3. effect of Mach number, J. Fluid Mech., 672(2011), 245-267.

[27] L. Duan and M. P. Martin, Direct numerical simulation of hypersonic turbulent boundary layers. part 4. effect of high enthalpy, J. Fluid Mech., 684(2011), 25-59.

[28] M. Lagha, J. Kim and J. D. Eldradge, et al, A numerical study of compressible turbulent boundary layers, Phys. Fluids, 23(2011), 015106.

[29] M. Lagha, J. Kim and J. D. Eldradge, et al. Near-wall dynamics of compressible boundary layers, Phys. Fluids, 23(2011), 065109.

[30] X. Liang, X. L. Li and D. X. Fu, Y. W. Ma, DNS and analysis of a spatially evolving hypersonic turbulent boundary layer over a flat plate at Mach 8. Sci. Sin-Phys. Mech. Astron., 42(2012), 282-293.

[31] X. Liang and X. L. Li, DNS of a spatially evolving hypersonic turbulent boundary layer at Mach 8, Sci. China-Phys. Mech. Astron., 56(2013), 1408-1418.

[32] Z. W. He, X. L. Li and X. Liang, Nonlinear spectral-like schemes for hybrid schemes, Sci. China–Phys. Mech. Astron., 57(2014), 753-763.

[33] X. L. Li and L. Yan. Optimized Sixth-order Monotonicity-Preserving Scheme by Nonlinear Spectral Analysis, Int. J. Numer. Methods Fluids, 73(2013), 560-577.

[34] X. Liang, X. L. Li and D. X. Fu, Y. W. Ma, Complex transition of double-diffusive convection in a rectangular enclosure with height-to-length ratio equal to 4, part 1. Commun. Comput. Phys., 6(2009), 247-268.

[35] F. M. White, Viscous fluid flow. McGraw-Hill, (1974), pages 367-380.

[36] G. N. Coleman, J. Kim and R. D. Moser, A numerical study of turbulent supersonic isothermal-wall channel flow, J. Fluid Mech., 305(1995), 159-183.

[37] P. Bradshaw, Compressible turbulent shear layers, Annu. Rev. Fluid Mech., 9(1977), 33-54.

[38] T. Cebeci and A. M. O. Smith, Analysis of Turbulent Boundary Layers, Academic Press Inc, New York (1974).

[39] J. Gaviglio, Reynolds analogies and experimental study of heat transfer in the supersonic boundary layer, Int. J. Heat Mass Transfer, 30(1987), 911-926.

[40] M. W. Rubesin, Extra compressibility terms for favre-averaged two-equation models of inhomogeneous turbulent flows, NASA Tech. CR(1990), Technical Report 177556.

[41] P. G. Huang, G. N. Coleman and P. Bradshaw, Compressible turbulent channel flows, DNS results and modeling, J. Fluid Mech., 305(1995), 185-218.

[42] S. K. Lele, Compressibility effects on turbulence, Annu. Rev. Fluid Mech., 26(1994), 211-254.

[43] D. X. Fu, Y. W. Ma, X. L. Li and Q. Wang, Direct Numerical Simulation of Compressible Turbulence, Science Press, Beijing(2010).

[44] A. A. Townsend, The Structure of Turbulent Shear Flow, Cambridge University Press, London(1976).

[45] S. J. Kline, W. C. Reynolds and F. A. Scheaub, et al, The structure of turbulent boundary layers, J. Fluid Mech., 30(1967), 741-773.

[46] H. P. Bakewell and J. L. Lumley. Viscous sub-layer and adjacent wall region in turbulent pipe flow, Pyhs. Fluids, 10(1967), 1880-1889.